
Supporting Information:

Radiation-Induced Helium Nanobubbles Enhance Ductility in Submicron-Sized Single-Crystalline Copper

Ming-Shuai Ding¹, Jun-Ping Du², Liang Wan¹, Shigenobu Ogata^{2,3}, Lin Tian¹, Evan Ma^{1,4}, Wei-Zhong Han^{1*}, Ju Li^{1,5*}, Zhi-Wei Shan¹

Experimental and simulation methods

Figures S1-S7

Table S1

Movies S1-S5

1. Synthesis of nano bubbled Cu by He implantation

In this study, we synthesized the nano bubbled copper (NB-Cu) sample by using helium implantation on an annealed coarse-grained (average grain size 20-30 μm) Cu TEM foil. In order to minimize other defects such as dislocation loops and adjust the size and distribution of bubbles, He implantation was conducted at a temperature of 450 $^{\circ}\text{C}$ with ion energy of 200 keV and achieved a fluence of 2×10^{17} ions cm^{-2} (more details in reference 1). The corresponding damage and He distribution can be calculated according to the stopping and range of ions in matter (SRIM) [2] as the blue and red curves shown in Fig. 1a. The cross sectional view of He bubbles distribution was also experimentally investigated through lift out technique, as the TEM image shown in Fig. 1a, which is perfectly consistent with the prediction by SRIM. The peak of the He concentration (He bubbles) is at 650 nm from the top surface. Only the region with high He concentration was selected and fabricated into submicron-sized samples for *in situ* tests, as the marked in Fig. 1a. As a result, the average He concentration for each NB-Cu sample will be slightly different from each other and varied from 3% to 8at.%.

2. *In situ* nano-mechanical testing.

The pillars were fabricated utilizing focus ion beam (FIB, FEI Helios Nanolab 600) with an accelerating voltage of 30 kV and an ion beam current of less than 28 pA for final machining. The NB-Cu sample for high resolution observation was firstly FIBed with final ion beam current of 1.5 pA and then further polished by using M1040 Nano Mill (Fischione Inc) with accelerating voltage of 800 V. *In situ* mechanical tests were conducted using a Hysitron PicoIndenter (PI95) inside a FEG JEOL 2100F transmission electron microscope (TEM, 200 keV). The displacement rate was programmed to be 3 nm/s for compression and 5 nm/s for tension. The tests were carried out under strain rate of $\sim 10^{-3}$ /s. All the movies of *in situ* tests were recorded in under focus imaging condition (-300 nm to -500 nm). The morphologies of the deformed pillars were characterized using a Hitachi SU6600 scanning electron microscope (SEM, 10 keV). After fabrication, the specimens were quickly transferred into the TEM to conduct the mechanical test. Prior to testing, pillars were carefully aligned with the diamond punch or tensile grip to ensure the uniaxial compression or tension. The whole deformation process of the specimens during loading was recorded by Charge-Coupled Device (CCD, Gatan 833) with frame rate of 10 frames per second. The bending test on NB-Cu cantilever was conducted under manual control with the piezo force instead of the displacement rate control.

3. Estimation of He bubble parameters in Cu

A NB-Cu thin film was micro machined by FIB with final ion beam current of 9.7 pA. The corresponding thickness t was carefully measured under the SEM imaging from the top view as shown in Fig. S1a. Then the thin foil was quickly transferred into a TEM in order to reduce the external contamination. Fig. S1b showed the typical TEM image of the He bubbles from which we can get the number of bubble, N , and the total bubble volume, V_{bubble} , in a specific area, s , by assuming the bubbles are spherical. Average He concentration of this film was estimated to be 5.5% according to the distance from the implanted surface and the He concentration shown in Fig. 1a. In this typical region, the bubble volume fraction $V_{fraction} = \frac{V}{s \times t}$ can be calculated to be 9.48% and the bubble spacing $l = \frac{1}{\sqrt{N \times d / (s \times t)}}$ was estimated to be 15.6 nm, where d is the average bubble diameter. He bubble pressure were estimated using a similar method as that in reference 3. For this specific region, the value of bubble pressure was estimated to be ~ 800 MPa. Therefore, we used a rough value of 1 GPa for the He bubble pressure in the paper.

4. MD simulations on the dislocation nucleation and dislocation-bubble interaction.

4.1 Calculation method of the activation free energy

To understand the dislocation nucleation governed deformation mechanism in Cu samples with and without He bubble, stress dependent activation free energies of dislocation nucleation from internal surface of He bubbles and sample's surface corner sites are computed using free end nudged elastic band (FE-NEB) method [4,5]. Here the large-scale atomic/molecular massively parallel simulator (LAMMPS) [6] code with our implementation of FE-NEB method is used. For the interatomic interactions, the Cu-Cu embedded-atom method (EAM) potential by Mishin *et al.* [7] and the He-He and He-Cu 2-body potentials by Kashinath *et al.* [8] are adopted. We used two atomic models for the activation free energy computations, such as He bubble and nanopillar models (See Fig.S6). The both models have the same dimensions of $X \times Y \times Z = 10.7 \text{ nm} \times 10.6 \text{ nm} \times 10.6 \text{ nm}$ along the Cu $[110]$, $[1\bar{1}2]$ and $[1\bar{1}\bar{1}]$ directions. The He bubble model contains one 5 nm spherical He bubble. Periodic boundary conditions (PBCs) are imposed along all the three directions in the He bubble model and imposed only along $[001]$ direction in the nanopillar model. The convergence criterion for the FE-NEB method is selected to be the force on the atoms less than 0.01 eV/\AA . The NEB spring constants are 1.0 and 0.01 eV/\AA^2 for He bubble and nanopillar models, respectively.

Shear stress τ_{yz} is loaded by applying shear strain γ_{yz} by means of displacing each $(1\bar{1}\bar{1})$ atomic plane to the $[1\bar{1}2]$ direction (Y direction). To avoid computation of He gas in the FE-NEB calculation, the 1 GPa bubble pressure acting on the internal surface of bubble is replaced by equivalent outward forces act on the surface atoms located within $\sim 5 \text{ \AA}$ from the surface of bubble. It should be noted that a $(1\bar{1}\bar{1})$ in-plane constraint to each atom is applied to the nanopillar model to avoid a rotation of model and thus to maintain the applied shear stress during the FE-NEB calculation.

Obtained stress dependent activation free energy of the dislocation nucleation at 0 K is fitted by using $\Delta G(\sigma) = A(1 - \frac{\sigma}{\sigma_{th}})^q$ [9], where A and q are fitting parameters. The σ_{th} is the athermal critical stress, which is directly obtained from the critical stress of dislocation nucleation by performing the shear simulations at 0 K. The fitting results are $A = 32.58 \text{ eV}$, $q = 3.76$ for the He bubble model and $A = 5.63 \text{ eV}$, $q = 1.70$ for the nanopillar model, and $\sigma_{th} = 2.73 \text{ GPa}$ and 2.80 GPa for the He bubble and the nanopillar models, respectively. The temperature effect on the activation free energy is assumed to be $\Delta G(\sigma, T) = A(1 - \frac{T}{T_{dis}})(1 - \frac{\sigma}{\sigma_{th}})^q$, where $T_{dis} = 700 \text{ K}$ is the disordering temperature for Cu surface. In this study, we use the same value of T_{dis} for the both He bubble and nanopillar cases. The dislocation nucleation frequency ν is computed by the Arrhenius equation using the $\Delta G(\sigma, T)$.

$$\nu = R_0 \exp\left(-\frac{\Delta G(\sigma, T)}{kT}\right),$$

where the pre-factor R_0 is product of number of equivalent nucleation sites N and trial frequency of nucleation event ν_0 . The number of equivalent nucleation sites on the internal surface of He bubbles and the surface corner sites of nanopillar are roughly estimated as $N_{bubble} = VN_V^{Bubble} f_V^{HS} n_{bubble}^{site} \sim 2 \times 10^3$ and $N_{pillar} = 4 \frac{L}{d} f_L^{HS} \sim 1 \times 10^2$, where $V = 2.4 \times 10^7 \text{ nm}^3$ and $L = 600 \text{ nm}$ are typical sample volume and length in the tensile direction. The $f_V^{HS} \sim \frac{1}{100}$, $f_L^{HS} \sim \frac{1}{100}$, and $N_V^{Bubble} \sim 7.6 \times 10^{-4} \text{ nm}^{-3}$ are volume fraction of the highest stress concentration regions in the sample, length fraction of the highest stress concentration parts along the edge line of the surface corners of the sample, and volume number density of He bubble of the sample, respectively. The local stress concentration may usually occur at around the fillet of the dumbbell-shaped samples. The $d = 0.21 \text{ nm}$ is the distance between adjacent Cu $\{111\}$ planes. The trial frequency ν_0 is estimated as $3 \times 10^{11} \text{ s}^{-1}$ for nanopillar model and $11 \times 10^{11} \text{ s}^{-1}$ for He bubble model from the free energy curvature along the MEP [6] at the initial equilibrium atomic configuration. It should be noted that,

since the sample corner edges may not be so atomistically sharp like in the nanopillar model, in actual experiment the dislocation nucleation frequency from the sample corner could be rather lower than our estimation.

4.2 Simulation of dislocation-bubble interaction

The mobility of dislocation and dislocation-bubble interactions are evaluated by MD simulations using the LAMMPS code as well. Size of the models is 61.5 nm×14.2 nm×13.8 nm. The crystallographic orientations of X, Y and Z axes are along [110], $[1\bar{1}2]$ and $[1\bar{1}\bar{1}]$, respectively. The PBCs are imposed on the X and Y directions. An edge dislocation along Y direction with Burgers vector $\mathbf{b} = [110]/2$ is initially placed in the middle of the model. After atomic relaxation at 300 K, the dislocation dissociates into two $1/6\langle 112 \rangle$ partials on $(1\bar{1}\bar{1})$ plane. For the model with He bubbles, three 5 nm He bubbles with 1 GPa He gas pressure inside are placed along X directions. The centers of bubbles are located on the dislocation glide plane. The MD shear simulations are performed at 300 K under constant shear stress. The shear stress τ_{xz} is applied by adding force on the upper and lower surface atoms within six $(1\bar{1}\bar{1})$ surface layers. Instead of direct measurement of dislocation glide distance, the relative average displacement between the upper and lower surface layers was used to indirectly estimate the average of dislocation glide distance. The mobility of dislocation glide in the models with and without He bubbles are shown in Fig. S7.

To demonstrate that the step on He bubble surface formed by dislocation cutting can act as new dislocation source, another MD shear simulation is performed. The simulation is performed at 300 K under constant shear strain rate $\dot{\gamma}_{xz} = 10^9 \text{ s}^{-1}$. The model size is 61.5 nm×14.2 nm×13.8 nm. The crystallographic orientations of X, Y and Z axes are along [110], $[1\bar{1}2]$ and $[1\bar{1}\bar{1}]$, respectively. The PBCs are imposed along all the three directions. Six 5 nm He bubbles with 1 GPa gas pressure are located in the model. An edge dislocation dipole with Burgers vector $\mathbf{b} = \pm[110]/2$ is inserted in the model. The edge dislocation cut the He bubble and made the step on He bubble surface, which can be new dislocation nucleation site (Fig. 5(c)).

Figure S1

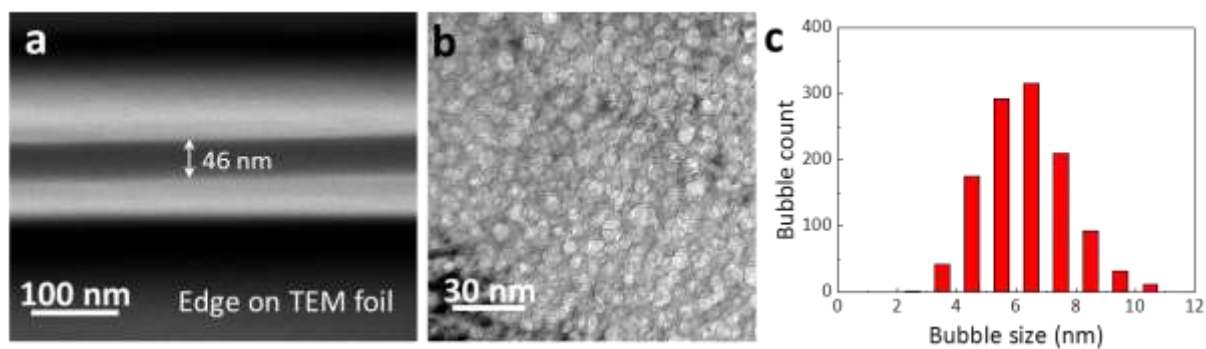


Fig. S1. A typical 46 nm thick NB-Cu thin foil used for measuring the bubble size and volume fraction. (a) Top-view of the foil thickness; (b) Plane-view of the bubble distribution; (c) Bubble size distribution in the NB-Cu foil.

Figure S2

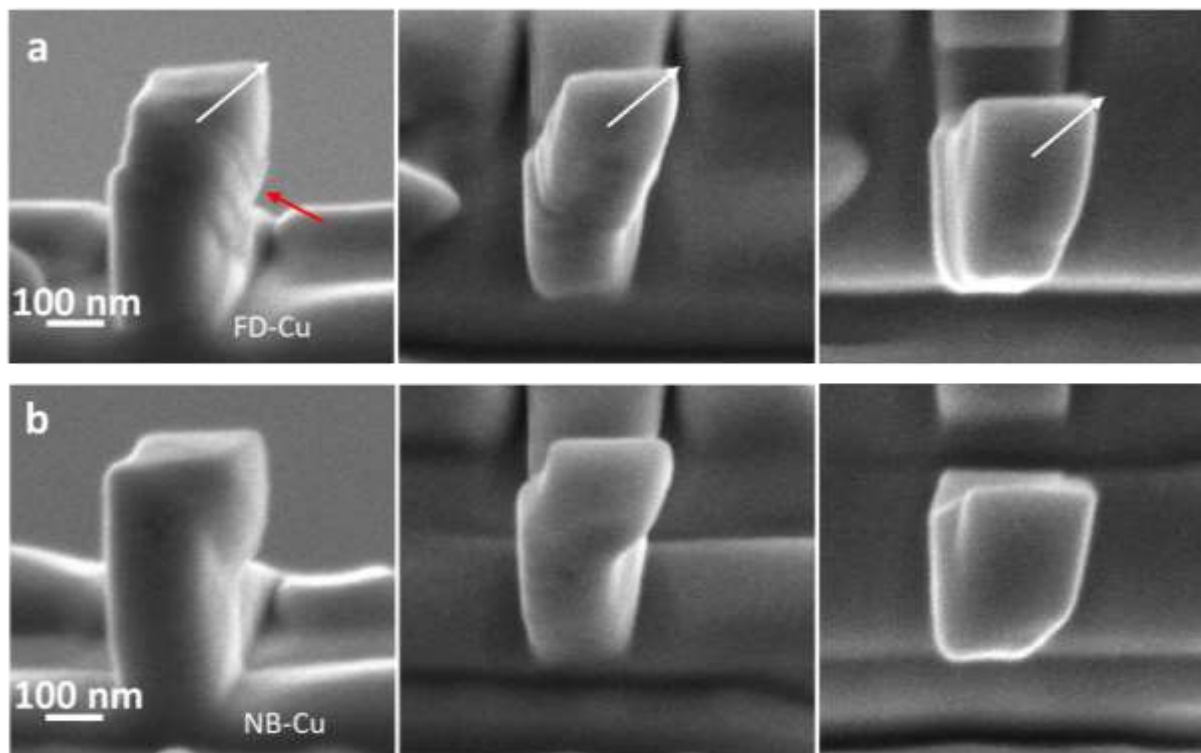


Fig. S2. Postmortem SEM observation of the compressed pillars shown in Fig. 2. Sharp slip steps can be identified in FD-Cu pillar, while only smooth deformation surface can be found in NB-Cu pillar. The top view of the deformed pillars ensured that no apparently sample buckling occurred during the compression.

Figure S3

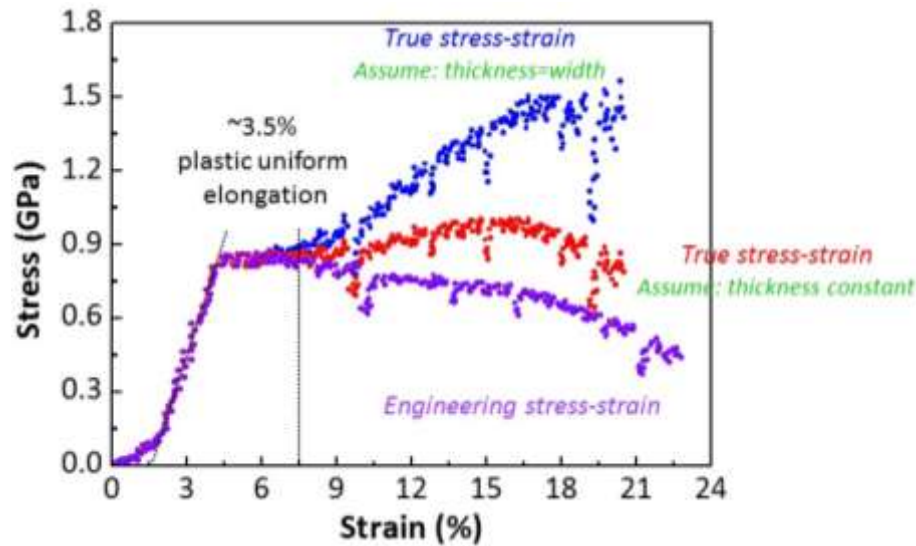


Fig. S3. Tensile stress-strain curves of the nano bubbled Cu pillar shown in Fig. 2. The variation of the width of the sample during tensile loading is measured from the in situ video. The true stress-strain curves were estimated in two conditions: case 1, assume the sample thickness is constant, as shown by the red data; case 2, assume the variation of sample thickness is proportional to the width during tension, see the blue data. The real true stress-strain curve should be at least lie in between these two cases.

Figure S4

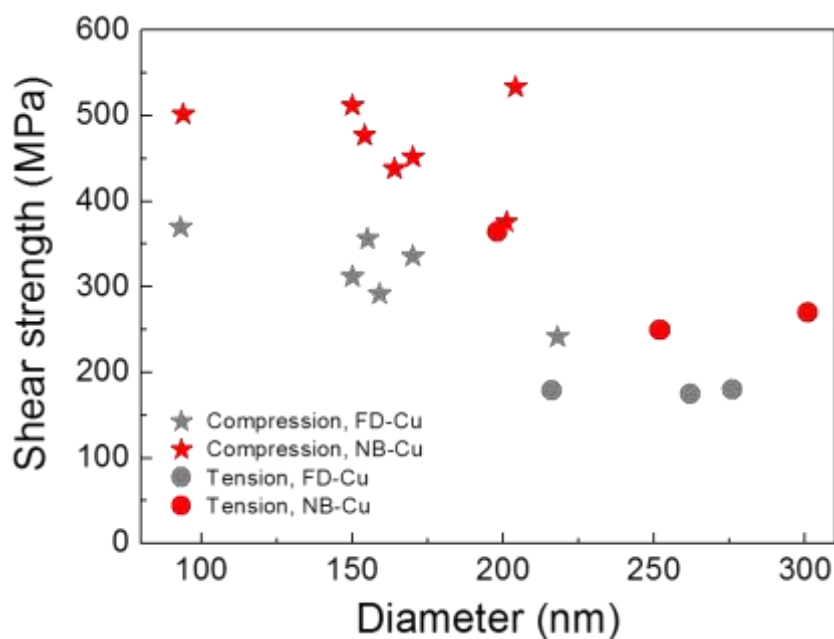


Fig. S4. Comparison of the shear strength of FD-Cu pillars with the nano bubbled Cu pillars under different loading directions and pillar size. Generally, the NB-Cu pillars showed higher shear strength compared with the FD-Cu under both compression and tension. Overall, the pillar size effect on the shear strength is not obvious but have slightly difference in tension and compression.

Figure S5

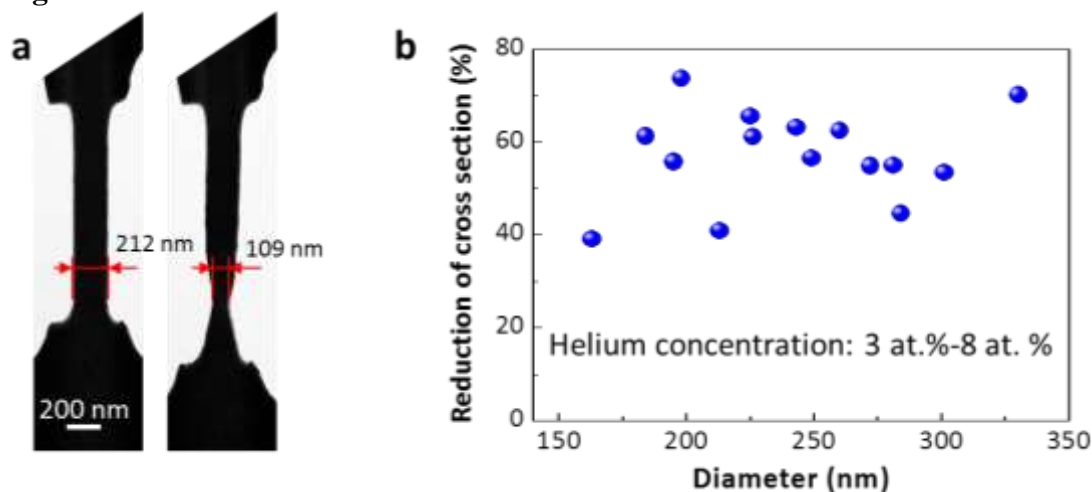


Fig. S5. Reduction of cross section of the nano bubbled pillars in tension. (a) The measurement of the width of tensile dog-bone sample prior to tension and at the moment just before fracture by using *in situ* video. (b) Reduction of cross section of the measured sample subject to tension by assuming that the thickness variation is proportional to that of the width measured. The He concentration was 3at.%-8at.% in the tested samples.

Figure S6

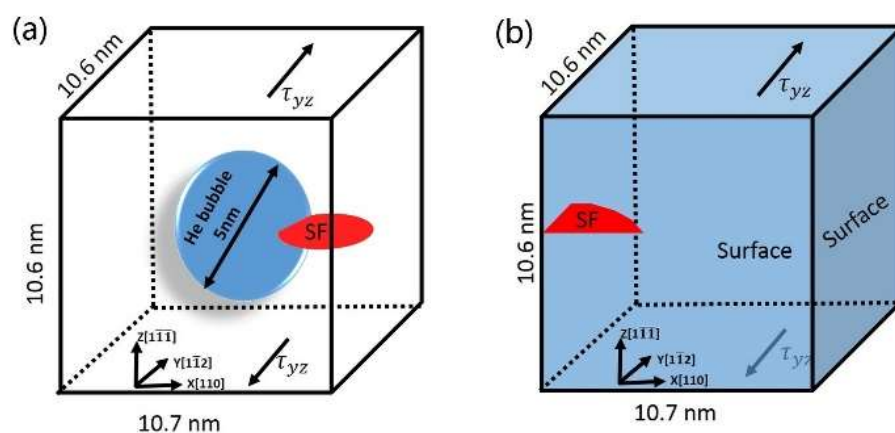


Fig. S6. Schematic diagram of dislocation nucleation from (a) He bubble and (b) surface of nanopillar. The red areas denote that stacking fault (SF) surrounded by the Shockley partial dislocation.

Figure S7

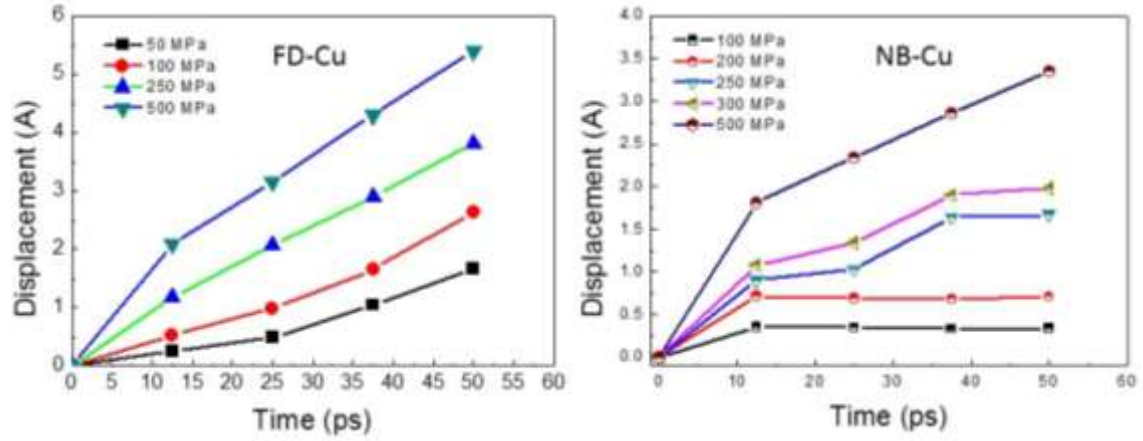


Fig. S7. The mobility of dislocations in FD-Cu pillar (a) and NB-Cu pillar (b) under different magnitude of shear stress calculated by MD simulations.

Table S1. Comparison of shear strength for the fully dense Cu (FD-Cu) and nano bubbled Cu (NB-Cu) with different loading directions.

Sample number	Loading direction	Sample size (nm)	Shear strength(MPa)	Loading type	Sample type
1	[751]	170	452	Compression	NB-Cu
2	[751]	170	336	Compression	FD Cu
3	[751]	170	452	Compression	NB-Cu
4	[751]	150	512	Compression	NB-Cu
5	[751]	150	312	Compression	FD Cu
6	[111]	94	502	Compression	NB-Cu
7	[111]	93	370	Compression	FD Cu
8	$[13 \bar{6} 1]$	164	438	Compression	NB-Cu
9	$[13 \bar{6} 1]$	159	292	Compression	FD Cu
10	$\bar{1}13$	154	477	Compression	NB-Cu
11	$\bar{1}13$	155	356	Compression	FD Cu
12	[211]	201	376	Compression	NB-Cu
13	[531]	218	242	Compression	FD Cu
14	[531]	204	534	Compression	NB-Cu
15	[122]	252	250	Tension	NB-Cu
16	[122]	276	180	Tension	FD Cu
17	[122]	301	270	Tension	NB-Cu
18	[122]	262	175	Tension	FD Cu
19	[311]	198	364	Tension	NB-Cu
20	[311]	216	179	Tension	FD Cu

Movies

Movie S1. Uniaxial tensile test of the NB-Cu sample.

Movie S2. Necking deformation of the NB-Cu sample.

Movie S3. Bending test of the NB-Cu sample.

Movie S4. Compression test on the NB-Cu pillar.

Movie S5. An edge dislocation interacts with a He bubble with 7 GPa internal pressure.

References

- [1] Han WZ, Demkowicz MJ, Fu EG, Wang YQ, Misra A. Effect of grain boundary character on sink efficiency. *Acta Materialia*, 60, 6341-6351, 2012.
- [2] Ziegler JF, Biersack JP, Littmark U. *The stopping and range of ions in solids*. New York: Pergamon Press, 1985.
- [3] Li N, Nastasi M, Misra A. Defect structures and hardening mechanisms in high dose helium ion implanted Cu and Cu/Nb multilayer thin films. *International Journal of Plasticity*, 32, 1-16, 2012.
- [4] Henkelman G, Uberuaga BP, Jonsson H. A climbing image nudged elastic band method for finding saddle points and minimum energy path. *The Journal of Chemical Physics*, 113, 9901-9904, 2000.
- [5] Zhu T, Li J, Samanta A, Kim HG, Suresh S. Interfacial plasticity governs strain rate sensitivity and ductility in nanostructured metal. *Proceedings of the National Academy of Sciences*, 104, 3031-3036, 2007.
- [6] Plimpton S. Fast parallel algorithms for short-range molecular dynamics. *Journal of computational physics*, 117, 1-19, 1995.
- [7] Mishin Y, Mehl MJ, Papaconstantopoulos DA, Kress JD. Structural stability and lattice defects in copper: Ab initio, tight-binding, and embedded-atom calculations. *Physical Review B*, 63, 224106, 2001.
- [8] Kashinath A, Demkowicz M J. A predictive interatomic potential for He in Cu and Nb. *Modelling and Simulation in Materials Science and Engineering*, 19, 035007, 2011.
- [9] Zhu T, Li J, Samanta A, Leach A, Gall K. Temperature and strain-rate dependence of surface dislocation nucleation. *Physical Review Letters*, 100, 025502, 2008.